Optimizing image-based patterned defect inspection through FDTD simulations at multiple ultraviolet wavelengths

Bryan M. Barnes*, Hui Zhou, Mark-Alexander Henn, Martin Y. Sohn, and Richard M. Silver
Engineering Physics Division, National Institute of Standards and Technology,
100 Bureau Drive MS 8212, Gaithersburg, MD, USA 20899-8212

ABSTRACT

The sizes of non-negligible defects in the patterning of a semiconductor device continue to decrease as the dimensions for these devices are reduced. These "killer defects" disrupt the performance of the device and must be adequately controlled during manufacturing, and new solutions are required to improve optics-based defect inspection. To this end, our group has reported [Barnes et al., *Proc. SPIE* 1014516 (2017)] our initial five-wavelength simulation study, evaluating the extensibility of defect inspection by reducing the inspection wavelength from a deep-ultraviolet wavelength to wavelengths in the vacuum ultraviolet and the extreme ultraviolet. In that study, a 47 nm wavelength yielded enhancements in the signal to noise (SNR) by a factor of five compared to longer wavelengths and in the differential intensities by as much as three orders-of-magnitude compared to 13 nm. This paper briefly reviews these recent findings and investigates the possible sources for these disparities between results at 13 nm and 47 nm wavelengths. Our in-house finite-difference time-domain code (FDTD) is tested in both two and three dimensions to determine how computational conditions contributed to the results. A modified geometry and materials stack is presented that offers a second viewpoint of defect detectability as functions of wavelength, polarization, and defect type. Reapplication of the initial SNR-based defect metric again yields no detection of a defect at λ = 13 nm, but additional image preprocessing now enables the computation of the SNR for λ = 13 nm simulated images and has led to a revised defect metric that allows comparisons at all five wavelengths.

Keywords: defect metrology, extreme ultraviolet, EUV, vacuum ultraviolet, VUV, deep ultraviolet, DUV, defect inspection, finite-difference time-domain, simulation, simulated imaging

1. INTRODUCTION

Semiconductor devices are the integral components of the ubiquitous electronic devices encountered in daily life. These devices (e.g., computer memory, central processing units (CPUs), etc.) are manufactured using multiple steps such as deposition, photolithography, and etching, with billions of transistors fabricated for a single device. There are several key parameters to monitor within these manufacturing processes. Monitoring the positioning offset of one photolithographically patterned layer with respect to the previous patterned layer is called overlay metrology, which is measured optically to sub-nanometer resolution using either scatterometry or imaging techniques. Measuring the width of the smallest features within these devices is called critical dimension (CD) metrology, and CDs can be measured by using scanning electron microscopy (SEM) or measured optically using model-based scatterometry. In manufacturing, currently, several devices are fabricated simultaneously on a 300 mm diameter silicon wafer, and sampling strategies are employed within a high-volume manufacturing environment to determine variations in overlay and CD across this wafer.

Meanwhile, this patterned layer must also be inspected for deviations from the nominal pattern that arise from manufacturing faults. Optics-based defect metrology specifically identifies locations on these wafers at which the printed pattern deviates from the designed pattern, specifically deviations that would lead to device failure due to shorted or broken electrical connections. Furthermore, if the undesirable changes in manufacturing conditions are systematic, then other devices on subsequent wafers may also have the same defects that continue to result in failed devices until the root cause is determined and resolved. These defects are called killer defects and the defining size characteristics of these defects grow smaller as the device sizes and critical dimensions continue to decrease. Stated differently, what previously may

*bryan.barnes@nist.gov; phone 1 301 975-3947; fax 1 301 975-4396; www.nist.gov

Barnes, Bryan; Henn, Mark Alexander; Silver, Richard; Sohn, Martin; Zhou, Hui.
"Optimizing image-based patterned defect inspection through FDTD simulations at multiple ultraviolet wavelengths."
Paper presented at Modeling Aspects in Optical Metrology, Munich, Germany. June 25, 2017 - June 29, 2017.

have been a tolerable patterning imperfection can become a killer defect as densities increase and CDs decrease in modern manufacturing.

The industrial methods of choice for inspecting for defects are optical, with some approaches opting for image-based solutions while other approaches favor detecting changes in light scattered off the sample. Optical methods yield the high speeds, the inherently parallel detection, and non-destructive measurements required for defect inspection, even as the defects remain unresolved. Typically, optical methods detect and locate defects for subsequent inspection and fault analysis using an SEM review.

The complex optical scattering interactions among patterned layouts and the layers upon which they are patterned defy simple explanation but important trends have been identified. It is well-understood in the industry, as shown in the literature [1], that with decreased dimensions, these killer patterned defects will scatter far less light thus complicating inspection. To heuristically describe the challenge of the optical inspection with these ever-decreasing defect sizes, comparisons have been made to Mie scattering. It is known that the intensity I scattered off spheres scales as $I \propto d^6/\lambda^4$ for a sphere with a diameter d and an inspection wavelength λ where $d << \lambda$ [2]. Again, defect scattering is not directly analogous to the scattering from spheres as the intended pattern and its substrate will also scatter and reflect light as well. However, the implications from this model are that the optical scattering from defects will be extremely difficult as dimensions continue to decrease, with CDs presently 14 nm and smaller.

From this model, however, decreasing the inspection wavelength offers a potential remedy to this acute manufacturing challenge. In a recent proceedings paper [3], we presented our initial results from a five-wavelength simulation study of the optical scattering from patterned defects in a fin layout, with wavelengths spanning the deep ultraviolet (DUV), the vacuum ultraviolet (VUV), and the extreme ultraviolet (EUV). Such fins are the basis of current three-dimensional Fin Field Effect Transistors (FinFETs). Simulations have been performed using a finite-difference time-domain (FDTD) [4] Maxwell's equations solver. As with our prior work [5, 6], the roles of incident angle, defect orientation, and polarization have been explored using the difference images resulting from subtracting an image without a defect from an image with a defect. This study establishes that up to a factor of five improvement over longer wavelengths may be realized in signal to noise ratio from the adoption of λ = 47 nm as an inspection wavelength. A shorter EUV wavelength, 13 nm, was ill-suited for defect inspection, yielding differential intensities as much as three orders of magnitude smaller than from simulations using λ = 47 nm. Wavelength-dependent optical constants are key to understanding these results. At λ = 47 nm, the materials exhibit metal-like optical constants while n and k for λ = 13 nm approach 1 and 0, respectively, for many materials. In addition, the defects are resolved at λ = 13 nm which leads to a highly localized signal that does not exceed the magnitude of the noise applied to the simulated images. A summary of this initial work is presented as Section 2 in this paper.

This proceedings paper explores possible computation-related causes for the disparity between the simulation results at 13 nm and 47 nm wavelengths, illustrating the inherent requirements upon FDTD modeling at multiple ultraviolet wavelengths for optimizing patterned defect metrology. It was noted in Ref. [3] that additional work remained to make the results more practical, such as the addition of line edge roughness and simulations with more process stacks. Our in-house developed FDTD code is tested quantitatively in two dimensions (2-D) simulating the reflection from a substrate with the computed polarization- and angle-resolved reflectivities then compared against values obtained using the well-known Fresnel equations. This test allows a qualitative check of the results obtained thus far at λ = 13 nm and λ = 47 nm. A modified fin geometry is introduced that better represents industrially relevant design and allows further testing of the FDTD code in three-dimensions (3-D) and further validation of the observed trends. Two important simulation parameters, the cubic grid size Δs and the simulation domain size are varied to seek conditions that will yield greater consistency in the simulation results. While defects at λ = 13 nm are again not readily apparent when applying the initial defect metric upon on preliminary defect simulations using this geometry, methods for improving the preprocessing of the differential image and modifying the defect metric are presented that yield comparisons across the full wavelength range.

2. REVIEW OF INITIAL SIMULATION STUDY

Methods, considerations, and results of our group's initial simulation study at five wavelengths (13 nm, 47 nm, 122 nm, 157 nm, and 193 nm) are summarized in this section. Full details appear in a recent proceedings paper [3].

2.1 Simulation study methodology

The goal of this initial study has been to quantify defect detectability as functions of incident angle, polarization, defect type, and wavelength. Finite-difference time-domain (FDTD) calculations of the electromagnetic field scattered from the patterned layout and its defects can yield images obtained through modeling of the Fourier optics at each of the five simulation wavelengths. The patterned layout is based upon public information about recent manufacturing processes [7, 8] while scaling features to make the silicon lines 8 nm wide, and are shown schematically in Fig. 1(a) and 1(b), with defects defined in Fig. 1(c). These bridging defects are commonly referred to by their SEMATECH[1] naming scheme: "Bx" and "By" defects. The defects are also 8 nm wide silicon lines, less than 40 nm in length and conformally coated. Incident angles are indexed using polar and azimuthal angles, θ and ϕ, as defined in Fig. 1(d). Simulations are performed with the plane wave illumination linearly polarized either perpendicular to or within the plane of incidence, and these results are used to calculate the effects of linearly polarized light that is oriented with respect to the sample patterning (e.g., X polarization, Y polarization). The materials used in this example are listed in Fig. 1(a) and their wavelength-dependent optical constants appear as Table 1.

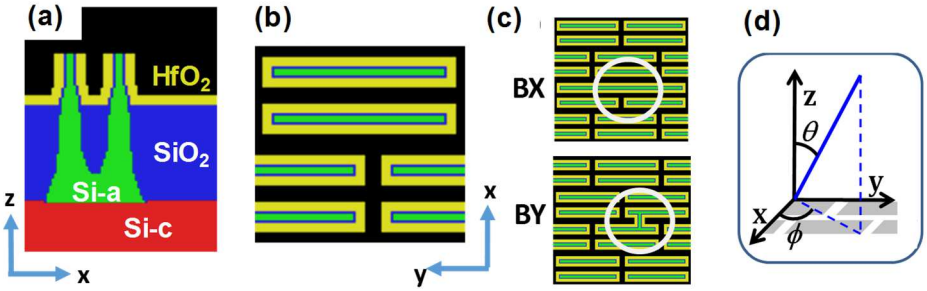

Figure 1. (a) *xz* cross section of fin pair modeled upon a transmission electron micrograph in Ref. [8]. Materials shown were chosen from analysis of the public literature. (b) *xy* cross section through the fins. Image is of one unit cell (UC). (c) *xy* cross-sections showing bridge defects "Bx" and "By" within a 2 UC × 2 UC area. Note, the length of the "Bx" bridge runs along the *y* direction in our coordinate system, and the length of "By" runs along the *x* direction. (d) Coordinate system for simulated incident plane wave linear polarization axis and angle of incidence, both polar θ, and azimuthal, ϕ.

Table 1. Optical constants *n* and *k* for four key materials used in semiconductor manufacturing, as found in the literature.

λ (nm)	a-Si		c-Si		SiO_2		HfO_2	
	n	*k*	*n*	*k*	*n*	*k*	*n*	*k*
13	1	0.02	1.03	0.00113	0.98	0.01	0.97	0.0157
47	0.88	6.58	0.803	1.78	0.62	0.30	0.58	0.06
122	0.44	1.10	0.295	1.32	2.62	0.93	1.59	1.69
157	0.67	1.63	0.49	2.04	1.80	0	2.36	1.22
193	0.98	2.11	0.88	2.80	1.66	0	2.98	0.43
Refs.	[9]		[10]		[11-13]		[14]	

A guiding consideration in the simulation of defects is that the patterned structure can often be treated as periodic for the purposes of calculation. Periodicity removes possible unintended effects upon the scattered field from inadequate construction of perfectly matching layers (PMLs) around the sides the simulation domain, which are especially problematic

[1] Certain commercial materials are identified in this paper in order to specify the experimental procedure adequately. Such identification is not intended to imply recommendation or endorsement by the National Institute of Standards and Technology, nor is it intended to imply that the materials are necessarily the best available for the purpose.

when using several oblique angles of incidence at five different wavelengths. However, it is possible for defects to interact optically with their periodic copies if the domain size is too small. To minimize this source of error, one defect-containing unit cell (UC) should be placed within a buffer of non-defect containing UCs that will fill the rest of the simulation domain. In this initial study, the domain size was scaled such that the *x* and *y* domain sizes were at least 10 λ in length with a constant *z* size of 320 nm. The simulation domain lengths and widths for these five wavelengths are provided in Table 2.

For this study, obtaining numerical convergence for the simulations using λ = 13 nm proved difficult when using a 32-byte long floating-point data type, as the amplitude of the scattered field was on the order of the numerical noise in that simulation. For the 13 nm and 47 nm wavelengths, a 64-byte long floating-point data type was used instead, lengthening simulation times and increasing memory requirements. Also, this implementation of the FDTD uses equally sized cubic grids throughout the simulation domain to minimize potential sources of error from adaptive meshing; the cubic grid size, Δs, was set to yield integer widths of the fin dimensions while also maintaining $\Delta s < \lambda/10$. These values also appear in Table 2.

Table 2. FDTD domain size and cubic grid size. Cubic grid size corresponds to the length of one side of a cube used in the simulations, with Δs=2 nm leading to a cube 8 nm^3 in volume.

λ (nm)	*x* (nm)	*y* (nm)	Δs (nm)
13	672	720	1
47	1344	1344	1
122	1344	1260	2
157	1680	1800	2
193	2016	1980	2

Shown in Fig. 2 is a representative example of a simulated image and a simulated difference image. The image in Fig. 2 corresponds to λ=13 nm, normal incidence, X polarization imaging a "By" defect. The difference image is obtained by simulating the same patterned structure without the defect and subtracting its image from the image of the defect. In the absence of noise, these defects are observable. Noise was later added to this analysis through the inherent Poisson noise of the detectors, an important concern for detectors with low photon flux. This noise depends upon the number of photons per pixel at the sensor. A conservative estimate was made in Ref. [3] that yielded 6400 photons per pixel for each measurement, independent of wavelength. Using this value allowed the application of Poisson noise to each individual pixel. Representative images with added noise appear in Fig. 3.

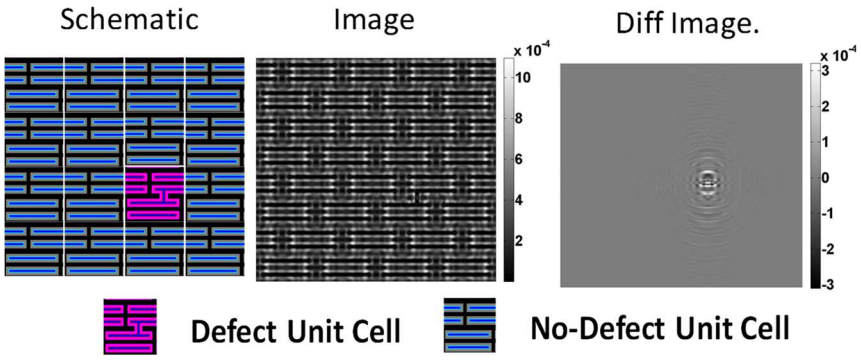

Figure 2. Schematic, simulated image, and difference image for a "By" defect. At λ = 13 nm, the simulation domain was populated with by a 4 × 4 array of unit cells (UC) with one UC containing a defect, guarantee at least 10 λ separation between the edges of the simulation domain. Wavelength-dependent domain sizes are provided in Table 2. The image is simulated assuming normal incidence and X linear polarization. The difference image is determined by subtracting the image of a pattern with no defect (not shown) from this image with the defect shown.

2.2 Defect metric definition

A primary concern for such a simulation study that considers five different wavelengths is the establishment of a defect metric that is applicable for all wavelengths, domain sizes, and cubic grid sizes. Utilizing the absolute value of the differential image (AVDI), an ideal candidate for this defect metric is a signal to noise ratio, defined here as

$$SNR = \frac{I_{\text{signal}}}{\sigma_{\text{noise}}}, \tag{1}$$

where I_{signal} corresponds to the total intensity gathered due to the defect while σ_{noise} is the standard deviation of the intensities at all pixels falling below certain thresholds; the latter is not to be confused with σ, the standard deviation of the AVDI, as it is a 5σ threshold is initially used to differentiate the pixels with large intensities due to the defect from those pixels with a smaller signal from the defect or the applied noise. In Fig. 3, two examples are shown to illustrate the calculation of the signal-to-noise ratio. The first column shows the application of this 5σ thresholding on the AVDI. With noise, some of this signal comes from the optical response from the defect and from outlying pixels that exceed the threshold. The second column demonstrates how an area threshold can separate this random noise from the defect signal. In this initial simulation study, a simple area threshold of A_{min} = 1000 nm^2 was sufficient. In the third column, pixels colored in green are averaged to determine I_{signal}. The standard deviation of the pixel intensities for the red pixels determines σ_{noise}. For a given combination of incident angle, polarization, defect type, and wavelength a signal to noise ratio can be calculated.

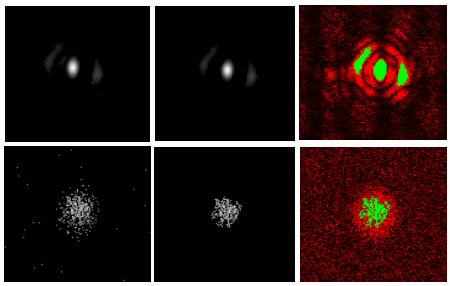

Figure 3. Application of intensity and area thresholding to separate a defect signal from its noise. The top and bottom rows are examples from λ = 47 nm and λ = 122 nm, respectively. The left column shows pixels with intensities exceeding 5σ. The center column shows the exclusion of areas less than a constant minimum area A_{min}. The right column shows the differential image due to the defect in green with the noise in red, permitting a signal to noise ratio to be determined from a single differential image.

2.3 Comparisons among wavelengths, polarizations, incident angles, and defect types

The key SNR results from the simulation study are presented as Fig. 4. SNR is plotted using polar plotting with interpolation that is based upon simulation results from 13 different angles of incidence. This presentation allows for comparisons among wavelength, defect type, polarization, and incident angle. For example, angle-resolved illumination positively affects the defect detectability of the "By" defect using X polarization at λ = 47 nm, with a polar angle of θ = 15° and azimuthal angle of either ϕ = 30° or ϕ = 60° both yielding optimized signal to noise values for this defect.

From these data, λ = 47 nm is the optimal wavelength for defect detection, outperforming λ = 122 nm by a factor of five or more. Minimal gains are observable decreasing the wavelength from λ = 193 nm to λ = 122 nm. A lack of appreciable signal even at large polar angles of incidence (i.e., small grazing angles) at 13 nm should be noted as it was anticipated that these might have yielded defect detectability. The optical constants $n(\lambda)$ as shown in Table 1 are near or at unity at 13 nm, while $k(\lambda)$ is near zero at that wavelength. As noted in our prior work, there is not a single combination of angle of incidence and polarization that is optimal for these defect types. In Fig. 4 the "Bx" defect is shown with the Y polarization while the "By" defect is shown with the X polarization. The bridging directions of these two defects are orthogonal to each other and in both cases, the polarization that optimizes detection runs parallel to the bridging direction (i.e. its longer axis.)

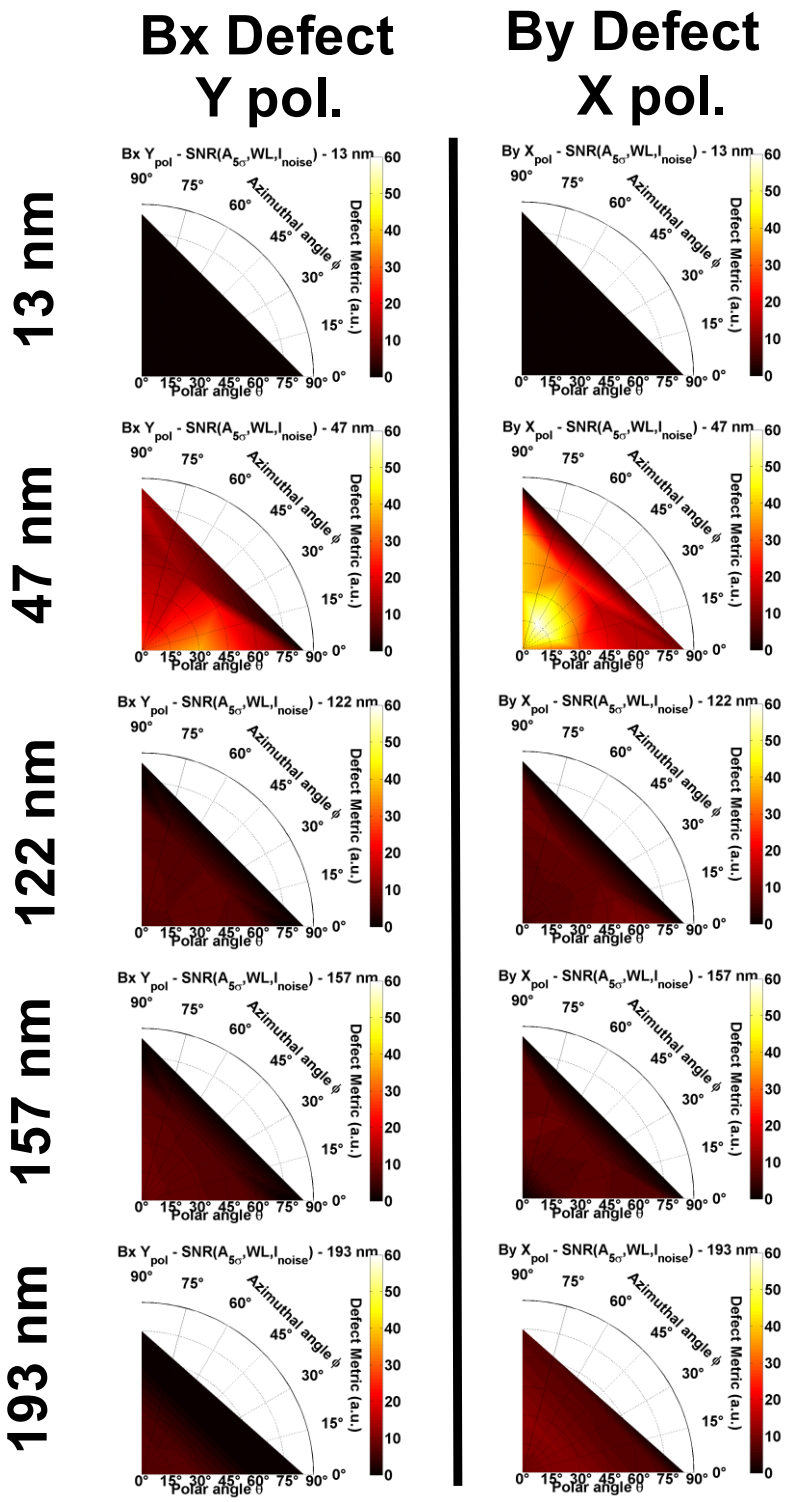

Figure 4. Signal to noise defect metric, plotted in polar plots showing the effects of polar and azimuthal angle, as functions of polarization and wavelength for the "Bx" defect, Y polarization (left) and the "By" defect, X polarization (right). For each column, the linearly polarized illumination is aligned with the direction of the defect, improving detectability for $\lambda \geq 47$ nm. With this defect metric, $\lambda = 47$ nm yields the greatest defect detectability.

Barnes, Bryan; Henn, Mark Alexander; Silver, Richard; Sohn, Martin; Zhou, Hui.
"Optimizing image-based patterned defect inspection through FDTD simulations at multiple ultraviolet wavelengths."
Paper presented at Modeling Aspects in Optical Metrology, Munich, Germany. June 25, 2017 - June 29, 2017.

3. ASSESSING FDTD PERFORMANCE ACROSS MULTIPLE WAVELENGTHS

Two trends were identified in the initial simulation study: a five-fold increase in the SNR for $\lambda = 47$ nm compared to longer wavelengths, and a decrease in the differential intensity of about three orders-of-magnitude for $\lambda = 13$ nm compared to $\lambda = 47$ nm. This section addresses how computational factors intrinsic to our implementation of a FDTD Maxwell's equations solver influence these trends. The optical constants shown in Table 1 vary greatly among the wavelengths, and the accuracy of the code across this wavelength range should be investigated at multiple angles, either to verify the accuracy of the code or to estimate possible systematic bias in the results. It is essential to understand the interplay among the cubic grid size, the domain size, computational capabilities, and simulation wavelength upon simulation accuracy.

3.1 Testing of two-dimensional FDTD using Fresnel equations

The initial simulation study has calculated images of patterned structures and their defects using the geometry shown in Fig. 1 and the wavelength-dependent optical constants in Table 1. The scattering from these features and the reflectivity of the constituent materials are inseparable within images, but an understanding of the FDTD-calculated reflectivity of these materials can be gained through comparisons against Fresnel equations. This first assessment here compares two-dimensional FDTD calculations of reflectivity from an unpatterned surface with the known polarization-dependent reflectivity of these materials. These simulations are functions of angle of incidence, optical properties, wavelength, and cubic grid size.

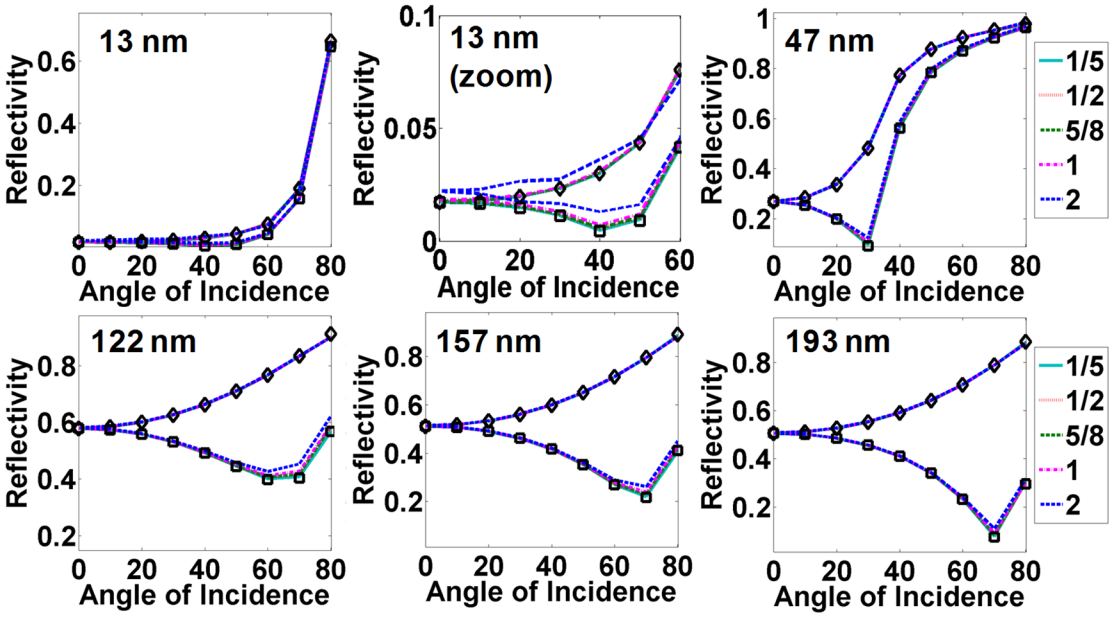

Figure 5. Reflectivity of HfO_2 as calculated using Fresnel equations (markers) and FDTD (lines) in a two-dimensional configuration, using one of five cubic grid sizes Δs: 1/5 nm, 1/2 nm, 5/8 nm, 1 nm, and 2 nm. The *s* polarization is the set of curves with diamond markers, the *p* polarization is the set of curves with square markers.

Figure 5 shows the reflectivity from HfO_2 for the five simulation wavelengths. This material is presented first as a HfO_2 film 8 nm thick coats the sides of the fins and the top of the SiO_2 in Fig. 1. For each wavelength, multiple values of Δs are calculated, with five presented here: 0.2 nm, 0.5 nm, 0.625 nm, 1 nm, and 2 nm. Each panel shows the Fresnel equation values for *s* polarization (diamond markers) and for *p* polarization (square markers). In each panel, the FDTD yields more accurate answers for the *s* polarization than for the *p* polarization across the range of incident angles and cubic grid sizes. For the *p* polarization, cubic grid size reductions are required to approach the known values. Discrepancies in the FDTD simulation are most apparent at those angles at which the reflectivity for the *p* polarization is lowest. This result follows naturally from the polarization of the light. The *s*-polarized illumination has its electric field vector parallel to the interface between the vacuum and the HfO_2 and maintains its orientation at the interface. In contrast, the *p*-polarized illumination has its electric field vector in the plane of incidence and thus is at some angle to the interface of the vacuum and the HfO_2.

Quantifying the percent error between the FDTD and the Fresnel equations is one possible method for identifying potential systematic errors in the three-dimension patterned defect simulation studies across several wavelengths given the HfO_2 coating in the initial simulation geometry. The initial simulation study used Δs = 1 nm for wavelengths of 13 nm and 47 nm, Δs = 2 nm for 122 nm, 157 nm, and 193 nm, and it is these grid sizes that are compared. For the *s* polarization, the percent error is less than 1 % for those cubic grid sizes for all incident angles and all wavelengths. The results for the *p* polarization must be described in more detail, as can be inferred from the "13 nm (zoom)" panel of Fig. 5. For Δs = 1 nm and λ = 13 nm, the largest percent error as a function of incident angle is about 55 % for both $\theta = 40°$ and $\theta = 50°$. (The percent error drops down to about 25 %, 20 %, and 5 % for Δs = 5/8 nm, 1/2 nm, and 1/5 nm, respectively.) The FDTD is over-estimating the reflectivity for *p*-polarized light systematically. For $\lambda \geq 47$ nm, the *p*-polarization FDTD reflectivity has percent errors near 1% for most of the angles of incidence, but each wavelength has angles at which the percent errors increase notably. The maximum percent error for the chosen grid sizes for HfO_2 is almost 20 % at $\theta = 30°$ for $\lambda = 47$ nm, 12 % at $\theta = 70°$ for $\lambda = 122$ nm, 21 % at $\theta = 70°$ for $\lambda = 157$ nm, and 45 % at $\theta = 70°$ for $\lambda = 193$ nm.

This 2-D FDTD evaluation suggests possible systematic bias in the accuracy of the images in the initial simulation study for images formed using *p*-polarized light. This corresponds to X polarization for $\phi = 0°$ and Y polarization for $\phi = 90°$, for example. However, this bias cannot account for the three-orders-of-magnitude change in the difference image intensity between λ = 13 nm and λ = 47 nm. It is more likely that the difference signal is highly localized at λ = 13 nm and does not strongly interact optically with the intended pattern. For $\lambda \geq 47$ nm, the defects and pattern are not resolvable and the combination of the pattern and the defect ultimately determine the scattering. As to the five-fold increase in signal-to-noise for λ = 47 nm compared to the longer wavelengths, note that the "By" defect has its strongest SNR in Fig. 4 at θ=15° at both $\phi = 30°$ and $\phi = 60°$, a polar angle at which the FDTD reflectivity is within 1 % of the known values and is thus sufficiently stable. Although there is some minor difference in Fig. 4 in the SNR between $\phi = 0°$ and $\phi = 90°$ for the "Bx" defect at $\theta = 30°$ and Y polarization, we have not yet established how a 20 % variation in the actual reflectivity could result in such a SNR increase, and in addition high SNR values are found for several other angle combinations for λ = 47 nm.

For completeness, reflectivity comparisons for the three other materials in the stack in Fig. 1 (SiO_2, a-Si, and c-Si) are provided at the end of this paper as Fig. 10. The FDTD and the *s* polarization again compare favorably while the grid size must be reduced to obtain better agreement between the *p* polarization FDTD results and the known Fresnel equation values. While discrepancies in accuracy exist, none of these appear to impact the findings of the initial simulation study.

Even as these discrepancies yield insight into systematic errors within these multi-wavelength FDTD calculations, they cannot fully take into consideration scattering interactions with a patterned layout. To test scattering interactions, the full three-dimensional FDTD code must be used with a defined pattern of interest.

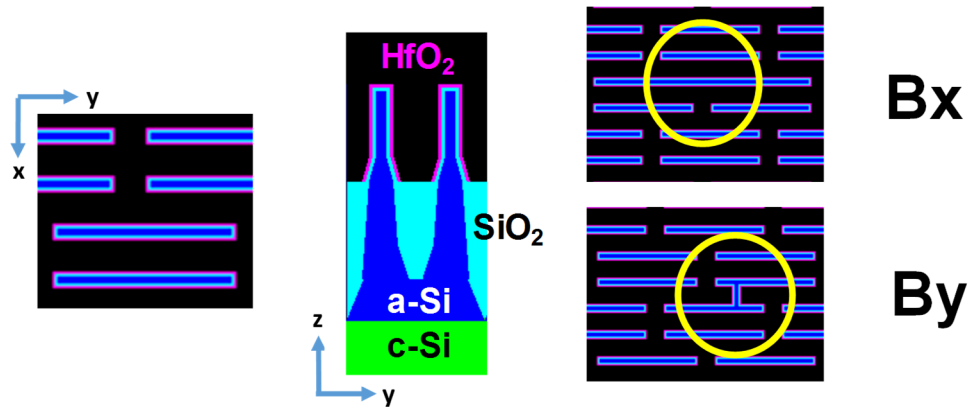

Figure 6. (left) *xy* cross-section through a fin layout modified relative to Fig. 1. Image is of one unit cell (UC). (center) *yz* cross-section of these fins, showing a 6 nm wide Si fin width in the fin with two conformal layers of SiO_2 and HfO_2, each 2 nm in thickness. (right) *xy* cross-sections showing bridge defects "Bx" and "By." As before, the length of the "Bx" bridge runs along the *y* direction in our coordinate system, and the length of "By" runs along the *x* direction.

3.2 Modifying the simulation geometry

The results of the initial simulation study should be viewed as specific to that materials stack and layout geometry. To further test trends in the scattering of patterned defects at multiple wavelengths, the simulation geometry has been altered as shown in Fig. 6. While the changes between the two figures may seem minor, several improvements may affect the scattered images. Foremost, the thickness of the HfO_2 conformal layer has been reduced from 8 nm to 2 nm and the placement of the HfO_2 has been localized to the fins only. There is no longer a conformal layer covering the SiO_2 layer. In addition, both the sides and tops of the fins are now covered with the conformal layers. The fin height has been increased from 42 nm to 52 nm relative to the SiO_2 layer and the Si fin width decreased from 8 nm to 6 nm to incorporate trends in the industry towards higher-aspect ratio fins [15]. The defects are also 6 nm wide silicon lines, less than 40 nm in length and conformally coated. Furthermore, the (x, y) coordinates specifying the vertices for the polygons defining these structures have been adjusted such that these coordinates could be evenly divisible by 2 nm, as much as practicable, to minimize possible rounding errors when using values of Δs as large as 2 nm. Rounding errors were reduced by reducing the fin pitch from 42 nm to 40 nm and changes in the unit cell size from 168 nm × 180 nm previously to 160 nm × 180 nm. Optical constants are unchanged.

3.3 Competing simulation requirements across multiple wavelengths

The 2-D tests of our in-house FDTD code showed improved accuracy with smaller cubic grid sizes. A case has been made in the initial simulation study for maintaining simulation domains for which the extent in x and y are at least 10 λ. However, cubic grid size and domain size are not the only considerations in performing these multiwavelength simulations.

The computing cluster upon which these simulations were performed has in general a maximum of 64 GB of memory per computing node. In Fig. 9, the total memory requirements of the 13 nm simulations are displayed to illustrate these constraints. Several combinations of large domain size and small cubic grid size cannot be realized within these memory requirements. In addition, simulations with λ = 47 nm have slightly larger memory requirements to account for the larger values of k at this wavelength, such that the simulation domain must be slightly reduced in the z axis to accommodate the combinations in Fig. 9. A similar assessment for the single precision (32-byte long floating-point data type) simulations for the VUV and DUV wavelengths leads to simulation domains as large as 10 × 10 for Δs = 1 nm, 6 × 6 for 2/3 nm grids, and 4 × 4 for 1/2 nm grids.

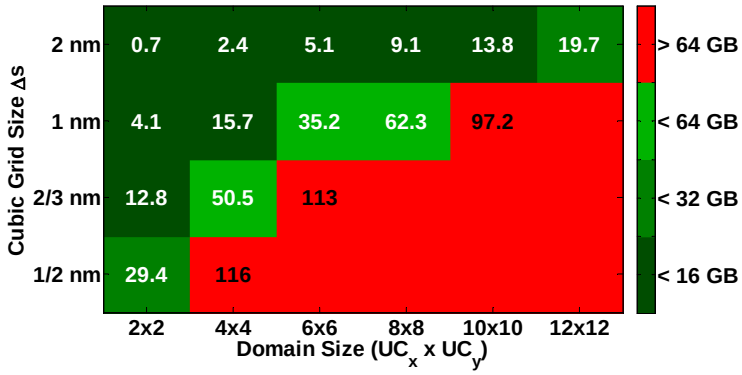

Figure 7. Memory requirements for performing FDTD simulations at λ = 13 nm with our in-house code on our local cluster, which in general has a limit of 64 GB total memory per node. Two simulations at 2 × 2, 1/2 nm can be run on a single node as each is less than 32 GB, while a 4 × 4, 2/3 nm simulation requires the entire node.

These requirements directly challenge capabilities to maintain 10 λ spacing on the domain size for longer wavelengths for grid sizes below Δs = 2 nm. Figure 8 shows the mean intensity of the "Bx" defect image with Y polarization using the 122 nm, 157 nm, and 193 nm simulation wavelengths as a function of domain size and cubic grid size. Use of a 2 nm grid, as was done at these wavelengths for the initial study, would yield an error in the mean intensity of no greater than approximately 5 % compared to Δs = 1 nm at all domain sizes. As expected, the mean intensity becomes more consistent as the domain size is increased. To allow for 10 λ × 10 λ domain sizes, these domain sizes had been set for the initial simulation study to be 8 × 7, 10 × 9, and 12 × 11 for 122 nm, 157 nm, and 193 nm wavelengths, respectively. Note that decreasing these domain sizes to 6 × 6 would lead to errors of less than 1 % in mean intensity for these three wavelengths.

Given these results and the known constraints, the results of the simulation study in Section 4 will feature Δs = 2/3 nm domain sizes of 4 × 4 for the EUV wavelengths and 6 × 6 for the VUV and DUV. In addition to improving the accuracy of the FDTD results for this defined geometry, reducing the cubic grid size will also allow the incorporation of line edge roughness (LER). Using 10 % of the CD as a guideline for defining the three-sigma value of the LER, $3\sigma_{LER}$ = 0.6 nm and this roughness will be better represented by Δs = 2/3 nm than by Δs = 1 nm. Cubic grid sizes of Δs = 0.5 nm and smaller are much less viable given our computational constraints as the maximum domain sizes available for λ > 13 nm are insufficient to yield accurate differential imaging results.

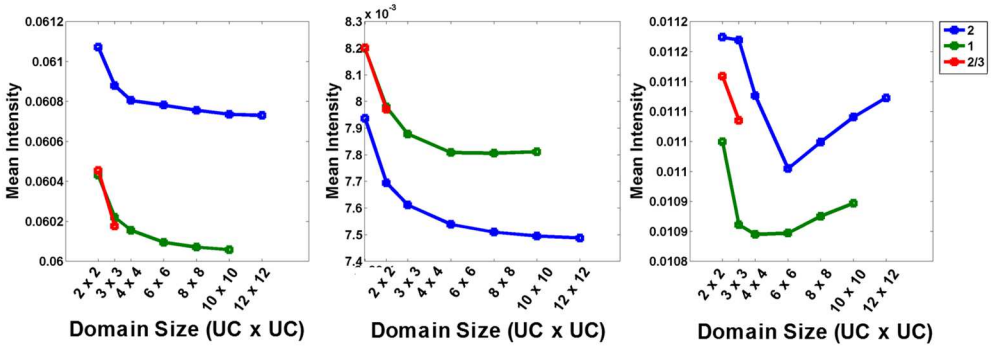

Figure 8. Mean intensity of the simulated "Bx" defect imaged using Y polarized light at normal incidence as functions of domain size and three cubic grid sizes Δs for the vacuum- and deep-ultraviolet wavelengths.

4. IMPROVING COMPARISONS AMONG WAVELENGTHS AND POLARIZATIONS

Motivation for and preliminary results from our group's current simulation study of the structure defined in Fig. 6 at the five wavelengths are presented below, with comparisons made with the initial simulation study in Section 2. This current simulation study is ongoing and full results will be presented in a subsequent publication.

4.1 Simulation study methodology

Goals for this new study are to quantify the defect detectability as functions of incident angle, polarization, defect type, and wavelength for patterns with and without line edge roughness (LER) and to validate trends observed in the initial simulation study. The addition of line edge roughness produces "wafer noise" which is extraneous signal in the difference images due to nuisance, non-killer deviations from the ideal patterning. Simulations with and without LER are to be performed to ascertain the wavelength dependence of the sensitivity to wafer noise and its effects on defect detectability. The same two bridging defects in Fig. 6, "Bx" and "By", are to be augmented with simulations of shorter non-bridging defects as well as line breaks. Definitions for the incident angles and polarizations persist from Fig.1, and the materials and their wavelength-dependent optical constants from Table 1 are once again used. For consistency and for improved convergence at 13 nm, the EUV wavelengths of 13 nm and 47 nm are to be simulated with a 64-byte long floating-point data type with the longer wavelengths calculated with a 32-byte long floating-point data type.

This study should add to our understanding of inspection capabilities at EUV wavelengths. It is important to determine if the trends in the initial study persist with minor changes in geometry, a re-arrangement of key conformal layers, and a smaller cubic grid size. Questions persist regarding the general trends in the EUV wavelengths: whether 13 nm is ill-suited for defect inspection and whether 47 nm wavelength is a clear improvement over longer wavelengths.

4.2 Comparisons between geometries for illumination at normal incidence

Preliminary simulation results from the current study are reported here and are limited to normal incidence illumination. Data from the initial study are presented as well for the two bridging defects in common, the "Bx" and "By" defects. Both are treated with the same defect metric as defined in Section 2.2 using a signal to noise ratio calculated after applying a 5σ threshold upon the absolute value of the differential image as well as an area threshold of A_{min} = 1000 nm^2. Results are shown in Table 3.

Considering first the current study, the defect is not recognized in not only for λ = 13 nm but also for λ = 193 nm and for "By" at λ = 122 nm. The lack of a definitive signal at 193 nm may be related to the reduction in the simulation domain

size, or the difficulties in separating the signal from the noise may be due to the small cubic grid size, as the images are produced with the pixel size matching the cubic grid size (e.g., 2/3 nm). Comparing the initial study to the current study, the dominance of λ = 47 nm is reaffirmed with exceptionally strong signals for the "By" defect with X polarization. However, there is only a factor of two difference between the "Bx", Y polarization SNR for λ = 47 nm in the current study.

Table 3. Comparison between the initial and current simulation studies using the initial signal to noise defect metric defined in Section 2.2. All values are for normal incidence illumination *N/A* indicates that no I_{signal} was isolated due to the defect.

λ (nm)	Initial Simulation Study		Current Simulation Study	
	"Bx" defect, X pol.	"By" defect, X pol.	"Bx" defect, Y pol.	"By" defect, X pol.
13	*N/A*	*N/A*	*N/A*	*N/A*
47	27.3	36.6	16.3	51.5
122	7.1	6.4	7.8	N/A
157	8.7	*N/A*	7.2	6.5
193	6.8	9.7	*N/A*	*N/A*

As to the loss of defect detectability at λ = 13 nm, the 2D FDTD assessment in Section 3 did show almost an order-of-magnitude difference in the reflectivity of HfO_2 between λ = 13 nm and λ = 47 nm, but this alone cannot describe the absence of defects at 13 nm here. In Ref. [3], it was stated that "[a]s the wavelength decreases, one might reasonably expect the optical scattering volume from a sub-resolved object to decrease, but for this study a simple area threshold of A_{min} = 1000 nm^2 was sufficient." This statement was made after assessing all the absolute value of the differential images (AVDIs) after the application of the Poisson noise, and as 13 nm wavelength images showed no clear defect-based signal, this area-based threshold was applied for the images for λ = 47 nm and longer wavelengths.

Having now reduced the likelihood that the lack of apparent defects using 13 nm was due to a systematic error in the FDTD or a particularly unfavorable materials stack, the focus now shifts to the application of the defect metric itself and its improvement for the challenge of capturing the signal to noise at λ = 13 nm and the equitable comparison of defect inspect across all five wavelengths.

4.3 Preprocessing of differential image data and modifying the defect metric

Calculating a defect metric using an AVDI is our standard practice and has been beneficial for four of the five wavelengths in both simulation studies here. It is anticipated that the area over which a difference would appear due to a 13 nm defect signal would be much smaller than those for the other defects and that it may reasonably have been lost with the application of Poisson noise. Additional processing of the AVDI would not tease out this small signal, so additional image processing has now been applied to the difference image before the application of the absolute value.

The amplitude of the Poisson noise is on par with the difference in intensity due to the defect. The mean intensity of the applied Poisson noise is zero, while the defect yields a non-zero difference in the absence of noise. To better isolate the defect signal, some averaging of the Poisson noise is required. Resizing the image effectively bins several of the smaller pixels to yield 1 larger pixel; areas of the image where the defect dominates will still have a non-zero mean while the noise will begin to average out. Figure 9 shows the effect of averaging upon the 13 nm differential image for the "Bx" defect with Y polarization. The final pixel size should be the same for direct comparison and will be 2 nm, the largest grid size used in either study. Thus, the 13 and 47 nm images in the initial study (Δs = 1 nm) are rescaled by a factor of 1/2, and all images in the current study are rescaled by a factor of 1/3 (Δs = 2/3 nm). Thus, results here are for simulated images with pixels that are 2 nm × 2 nm. Note for such pixel sizes, much work remains to make these results more practical.

The presence of a small but identifiable region in the rescaled AVDI for 13 nm requires an immediate reassessment of our existing quantitative defect metric. With this modification, the defects at 13 nm are identified areas of the defect's differential image that are greater than 40 nm^2, far less than the previous threshold of A_{min} = 1000 nm^2. Determining the optimal defect metric for these data is still a work in progress, as changes are very likely required when incorporating additional incidence angles, additional defect types, and LER. Therefore, for this publication, the defect metric is treated

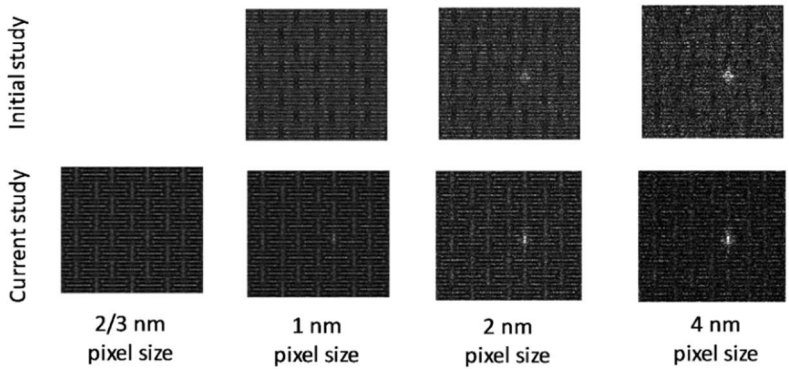

Figure 9. Changes in the AVDI with rescaling. The top row is for data from the original study with cubic grid size of 1 nm, the bottom row for the current simulation study with cubic grid size of 2/3 nm. The defect from the original study was not detected even with scaling to a 2 nm pixel size, but was for the current study due to this scaling to 2 nm.

as provisional. We envision applying machine learning techniques to better define the defect metric as more images are simulated.

For the moment, however, an intermediate threshold can be proposed using the comparative values of the largest contiguous area identified in the 5σ thresholding for the five wavelengths and two defect types as shown in Table 4. For wavelengths greater than 13 nm, these largest areas exceed the previous A_{min} threshold. It must be determined if a wavelength-dependent area threshold is required or whether it is adequate to simply set $A_{min} = 40$ nm^2. Based upon analyses of the largest area identified in each differential image and upon a qualitative, visual check of the differential images, the provisional defect metric is defined for these initial results as a 5σ threshold with an adjusted A_{min}. Lowering the threshold to $A_{min} = 40$ nm^2 or defining it as $A_{min}(\lambda) = 3\,\lambda$ both encompass the values listed in Table 4, but proper definition and further work are require to exclude as much of the noise as possible as well as capturing other defect-generated areas in the AVDI. For this provisional defect metric however, $A_{min}(\lambda) = 3\,\lambda$ was used. Note, it is yet to be determined whether this new defect metric adequately identifies wafer noise as background and not as defect signal.

There are SNR values for most every entry in Table 4 except for the "Bx" defect and Y polarized light at $\lambda = 13$ nm that was shown in Fig. 9. However, 13 nm wavelength and X polarization (not shown) was detectable with SNR = 6.7 with a largest area of 48 nm^2. Thus, the defect metric has been adjusted to accommodate the entire wavelength range. The VUV and DUV results show the effects of image scaling. For the initial study, the images are not scaled at all and the SNR ratios are the same as in Table 3. For the current study, scaling the image by a factor of 1/3 has brought out not only the defect at $\lambda = 13$ nm but also the defects at $\lambda = 122$ nm and $\lambda = 193$ nm.

Table 4. Comparison between the initial and current simulation studies using the provisional defect metric defined in Section 4.3. All values are for normal incidence illumination. *N/A* indicates that no I_{signal} was isolated due to the defect thus no SNR.

λ (nm)	Initial Simulation Study				Current Simulation Study			
	"Bx" defect, Y pol.		"By" defect, X pol.		"Bx" defect, Y pol.		"By" defect, X pol.	
	Largest Area above 5σ (nm^2)	Defect Metric	Largest Area above 5σ (nm^2)	Defect Metric	Largest Area above 5σ (nm^2)	Defect Metric	Largest Area above 5σ (nm^2)	Defect Metric
13	32	*N/A*	56	7.6	72	6.9	196	7.8
47	1800	41.5	376	53.7	2844	23.7	1480	57.8
122	4148	7.1	2052	6.4	6500	14.1	10096	10.2
157	10220	8.7	12	*N/A*	10588	14.4	13732	13.1
193	5356	6.8	13684	9.7	2588	6.4	15388	9.4

The scaling does not have an appreciable effect on the comparisons between the simulation studies. The SNR for the "Bx" defect in the current study is still is largest at λ = 47 nm by only around a factor of two, where the initial value is almost a factor of five larger at normal incidence. This trend will be watched as more angles are simulated. Like the initial simulation study, the "By" defect at normal incidence has a SNR that is between 4 and 5 times larger than the SNR of any other wavelength. Note that challenges remain in understanding these preliminary results, as the minimum area threshold differs significantly between the simulation studies as the threshold has been lowered to allow all five wavelengths to be accounted for by the provisional defect metric. Many additional checks are required and additional work is to be conducted to complete this current study and to place comparisons with the initial simulation study into proper context.

5. CONCLUSIONS

Simulation studies encompassing five wavelengths that range from the DUV to the EUV are being performed to determine the extensibility of defect metrology for ever-decreasing "killer" defects with sub-10 nm critical dimensions. An initial, full simulation study has recently been reported by our group and has been summarized here. In this initial study, λ = 47 nm showed better defect sensitivity by a factor of five as determined through a defined defect metric. This result is in stark contrast with the simulations for λ = 13 nm, as the difference image intensities for λ = 13 nm are about three orders-of-magnitude less than those for λ = 47 nm for the initial defined fin geometry.

In response to this initial study, a thorough FDTD consistency study has been presented as a check of these results and to quantify any possible sources of systematic bias in the simulations or other calculation steps that might affect the signal to noise. By comparing two-dimensional FDTD simulations of unpatterned substrates as functions of cubic grid size, angle of incidence, and wavelength, it was demonstrated that *s*-polarized reflectivities for our simulation conditions and in-house FDTD formulation are within 1 % of those determined analytically using Fresnel equations. For *p*-polarized reflectivities, there is a clear improvement in the consistency of the results with decreased grid sizes. Certain angles at each wavelength would lead to deviations in the FDTD-determined reflectivity as high as 55 % for λ = 13 nm using Δs = 1nm. The simulation accuracy of the full three-dimensional simulations is to be questioned, but these systematic deviations which always over-report the reflectivity do not appear to be the root cause of the differential intensity disparity between λ = 13 nm and λ = 47 nm. In addition, increased SNR at λ = 47 nm in the initial study is observable in simulations at angles of incidence for which the *p*-polarized reflectivity is sufficiently stable, with less than 1 % error. Therefore, it is not believed that these systematic biases in accuracy have affected the results of the initial study.

A modified three-dimensional geometry was introduced featuring higher aspect ratios and significant changes in the conformal layers. Whereas HfO_2 was the predominant material at the vacuum interface in the initial study, both HfO_2 and SiO_2 would be at on top of this materials stack. This geometry has been simulated using a variety of cubic grid sizes and domain sizes to determine the effects of changing these parameters on the mean intensity scattered from the patterned surfaces. Better consistency can be achieved by decreasing the cubic grid size, although this may practically necessitate the reduction of the domain size. Errors in the mean intensity due to shrinking the domain size proved to be less than 10 %, but reducing the domain size to below 10 λ x 10 λ requires additional study. FDTD consistency studies favored reducing the cubic grid size.

An additional factor, our desire to enable a second simulation study featuring line-edge roughness further motivates simulations of this new geometry with cubic grid sizes less than 1 nm^3. Preliminary results without LER have been presented and similar to the initial study, defects could be not be seen in the simulated, Poisson-noise added differential images for the 13 nm wavelength. However, additional preprocessing of the differential image enables isolation of the defect-based signal at this EUV wavelength. This result allows and requires the defect metric to be reassessed to accommodate all five simulation wavelengths. Applying a modified defect metric, the λ = 47 nm seems nearly as effective at detecting the "By" bridge defect as in the initial simulation study, although results for the "Bx" defect were less clear. Much work is to be performed to optimize the defect metric and to balance the simulation domain sizes, the cubic grid sizes, the computational resources, and this improved defect metric to more accurately and confidently address optimizing image-based patterned defect inspection.

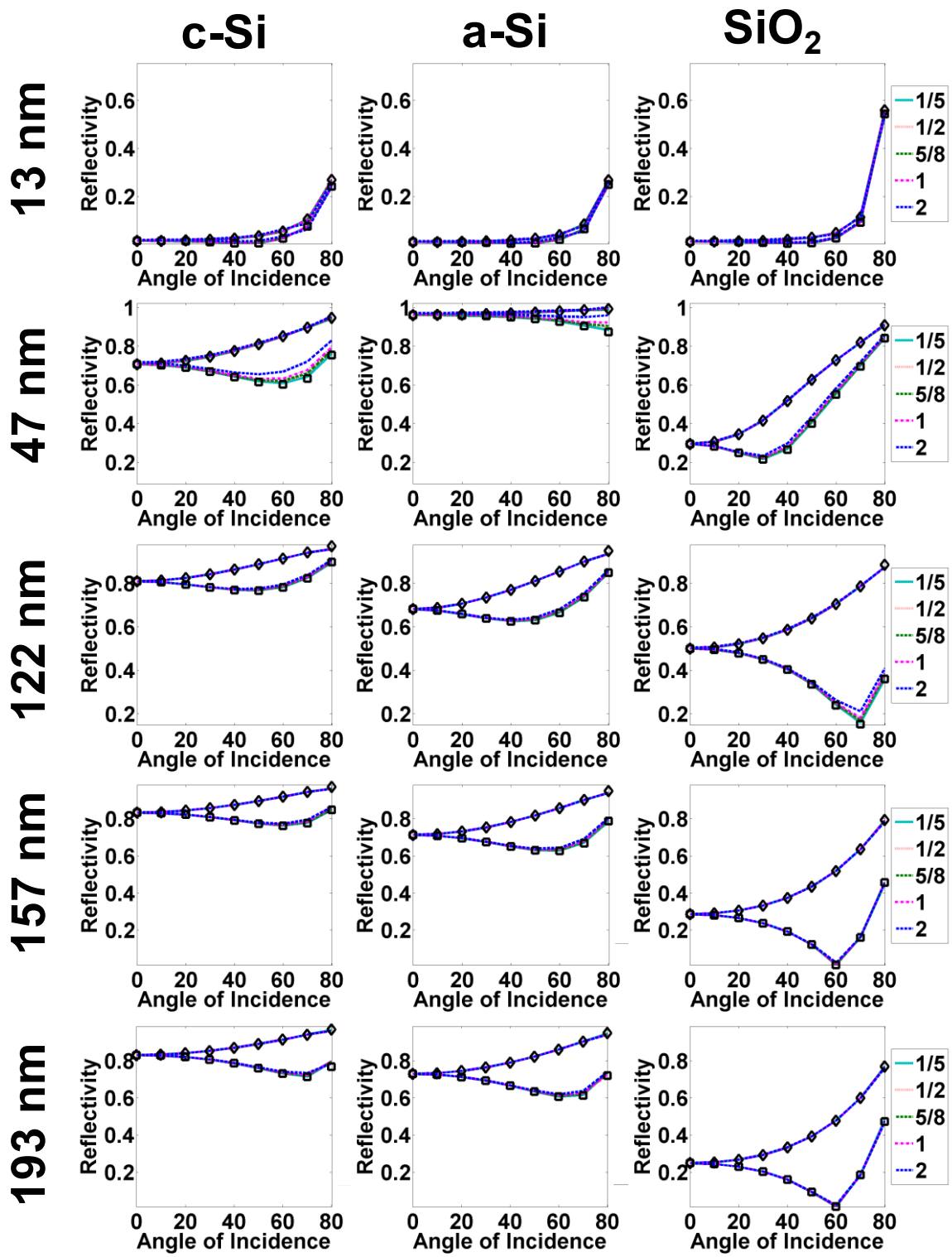

Figure 10. Reflectivity of SiO_2, a-Si, and c-Si as calculated using Fresnel equations (markers) and FDTD in a two-dimensional configuration, using one of five cubic grid sizes Δs: 1/5 nm, 1/2 nm, 5/8 nm, 1 nm, and 2 nm. The *s* polarization is the set of curves with diamond markers, the *p* polarization is the set of curves with square markers.

REFERENCES

[1] T. F. Crimmins, “Defect metrology challenges at the 11nm node and beyond,” Proc. SPIE, 7638, 76380H (2010). http://dx.doi.org/10.1117/12.846623

[2] M. I. Mishchenko, “Gustav Mie and the fundamental concept of electromagnetic scattering by particles: A perspective,” J. of Quant. Spectro. Rad. Trans., 110(14–16), 1210-1222 (2009). http://dx.doi.org/10.1016/j.jqsrt.2009.02.002

[3] B. M. Barnes, H. Zhou, M.-A. Henn *et al.*, "Assessing the wavelength extensibility of optical patterned defect inspection." Proc. SPIE, 10145, 1014516 (2017). http://dx.doi.org/10.1117/12.2262191

[4] A. Taflove, “Application of the Finite-Difference Time-Domain Method to Sinusoidal Steady-State Electromagnetic-Penetration Problems,” IEEE T. Electromag. Compat., EMC-22(3), 191-202 (1980). http://dx.doi.org/10.1109/TEMC.1980.303879

[5] B. M. Barnes, F. Goasmat, M. Y. Sohn *et al.*, “Effects of wafer noise on the detection of 20-nm defects using optical volumetric inspection,” J. Micro-Nanolitho. MEMS MOEMS, 14(1), 9 (2015). http://dx.doi.org/10.1117/1.jmm.14.1.014001

[6] B. M. Barnes, F. Goasmat, M. Y. Sohn *et al.*, “Enhancing 9 nm Node Dense Patterned Defect Optical Inspection using Polarization, Angle, and Focus,” Proc. SPIE, 8681, 86810E (2013). http://dx.doi.org/10.1117/12.2012250

[7] A. Raghunathan, S. Bennett, H. O. Stamper *et al.*, “13nm gate Intentional Defect Array (IDA) wafer patterning by e-beam lithography for defect metrology evaluation,” Microelec. Engr., 88(8), 2729-2731 (2011). http://dx.doi.org/10.1016/j.mee.2011.02.109

[8] S. Natarajan, M. Agostinelli, S. Akbar *et al.*, "A 14nm logic technology featuring 2nd-generation FinFET, air-gapped interconnects, self-aligned double patterning and a 0.0588 μm^2 SRAM cell size." 2014 IEEE Int’l Electron Devices Meeting (IEDM), 3.7.1-3.7.3 (2014). http://dx.doi.org/10.1109/IEDM.2014.7046976

[9] H. Piller, [Silicon (Amorphous) (a-Si)] Academic Press, Boston(1985). http://dx.doi.org/10.1016/B978-0-08-054721-3.50030-7

[10] D. F. Edwards, [Silicon (Si)*] Academic Press, Boston (1985). http://dx.doi.org/10.1016/B978-0-08-054721-3.50029-0

[11] E. Filatova, A. Sokolov, J.-M. André *et al.*, “Optical constants of crystalline HfO2 for energy range 140–930 eV,” Applied Optics, 49(14), 2539-2546 (2010). http://dx.doi.org/10.1364/AO.49.002539

[12] Q.-J. Liu, N.-C. Zhang, F.-S. Liu *et al.*, “Structural, electronic, optical, elastic properties and Born effective charges of monoclinic HfO2 from first-principles calculations,” Chinese Physics B, 23(4), 047101 (2014). http://dx.doi.org/10.1088/1674-1056/23/4/047101

[13] D. Franta, D. Nečas, I. Ohlídal *et al.*, “Dispersion model for optical thin films applicable in wide spectral range,” Proc. SPIE, 9628, 96281U (2015).

[14] H. R. Philipp, [Silicon Dioxide (SiO_2), Type α (Crystalline)] Academic Press, Boston (1985). http://dx.doi.org/10.1016/B978-0-08-054721-3.50039-3

[15] B. Bunday, E. Solecky, A. Vaid *et al.*, Proc. SPIE "Metrology capabilities and needs for 7nm and 5nm logic nodes." Proc. SPIE, 10145, 101450G (2017). http://dx.doi.org/10.1117/12.2260870

Barnes, Bryan; Henn, Mark Alexander; Silver, Richard; Sohn, Martin; Zhou, Hui.
"Optimizing image-based patterned defect inspection through FDTD simulations at multiple ultraviolet wavelengths."
Paper presented at Modeling Aspects in Optical Metrology, Munich, Germany. June 25, 2017 - June 29, 2017.